Tectonophysics 714–715 (2017) 21–30

Contents lists available at ScienceDirect

Tectonophysics

journal homepage: www.elsevier.com/locate/tecto

Source modeling of the 2015 Mw 7.8 Nepal (Gorkha) earthquake sequence: Implications for geodynamics and earthquake hazards

D.E. McNamara [a,]*, W.L. Yeck [a], W.D. Barnhart [b], V. Schulte-Pelkum [c], E. Bergman [e], L.B. Adhikari [d], A. Dixit [f], S.E. Hough [g], H.M. Benz [a], P.S. Earle [a]

[a] U.S. Geological Survey, National Earthquake Information Center, Golden, CO 80225, USA
[b] Department of Earth and Environmental Sciences, University of Iowa, Iowa City, IA 52242, USA
[c] Cooperative Institute for Research in Environmental Sciences, University of Colorado Boulder, 2200 Colorado Ave, Boulder, CO 80309-0399, USA
[d] Global Seismological Services, 1900 19th Street, Golden, CO 80401, USA
[e] National Seismological Centre, Department of Mines and Geology, Lainchaur, Kathmandu, Nepal
[f] National Society for Earthquake Technology - Nepal, Sainbu Residential Area, Ward 4, Bhaisepati, Lalitpur District, GPO Box: 13775, Kathmandu, Nepal
[g] U.S. Geological Survey, 525 S. Wilson Ave., Pasadena, CA 91106, USA

ARTICLE INFO

Article history:
Received 12 February 2016
Received in revised form 2 August 2016
Accepted 6 August 2016
Available online 15 August 2016

Keywords:
Gorkha earthquake
Aftershocks
Rupture model
Himalaya tectonics

ABSTRACT

The Gorkha earthquake on April 25th, 2015 was a long anticipated, low-angle thrust-faulting event on the shallow décollement between the India and Eurasia plates. We present a detailed multiple-event hypocenter relocation analysis of the Mw 7.8 Gorkha Nepal earthquake sequence, constrained by local seismic stations, and a geodetic rupture model based on InSAR and GPS data. We integrate these observations to place the Gorkha earthquake sequence into a seismotectonic context and evaluate potential earthquake hazard.

Major results from this study include (1) a comprehensive catalog of calibrated hypocenters for the Gorkha earthquake sequence; (2) the Gorkha earthquake ruptured a ~150 × 60 km patch of the Main Himalayan Thrust (MHT), the décollement defining the plate boundary at depth, over an area surrounding but predominantly north of the capital city of Kathmandu (3) the distribution of aftershock seismicity surrounds the mainshock maximum slip patch; (4) aftershocks occur at or below the mainshock rupture plane with depths generally increasing to the north beneath the higher Himalaya, possibly outlining a 10–15 km thick subduction channel between the overriding Eurasian and subducting Indian plates; (5) the largest Mw 7.3 aftershock and the highest concentration of aftershocks occurred to the southeast the mainshock rupture, on a segment of the MHT décollement that was positively stressed towards failure; (6) the near surface portion of the MHT south of Kathmandu shows no aftershocks or slip during the mainshock. Results from this study characterize the details of the Gorkha earthquake sequence and provide constraints on where earthquake hazard remains high, and thus where future, damaging earthquakes may occur in this densely populated region. Up-dip segments of the MHT should be considered to be high hazard for future damaging earthquakes.

1. Introduction

In this paper we calculate rupture characteristics of the 25 April 2015 Mw 7.8 Gorkha, Nepal mainshock and determine multiple-event relocated hypocenters for the aftershock sequence using a combined network of local, regional and global seismic stations (Dixit et al., 2015; Adhikari et al., 2015; Hayes et al., 2015). We find that aftershocks occur in regions surrounding the mainshock rupture maximum slip at depths consistent with the Main Himalayan Thrust (MHT) and below in the subducting Indian plate. In addition, the near surface portion of the MHT south of Kathmandu is primarily absent of aftershocks and slip during the mainshock. Results from this study characterize the details of the Gorkha earthquake sequence, provide constraints on the geodynamics of the India-Eurasia continental collision zone, and suggest where earthquake hazard remains high in this densely populated region.

1.1. Tectonic setting

Approximately 65 million years ago, final subduction of Tethyan oceanic crust occurred as the northward converging Indian plate collided with the southern margin of Eurasia at a relative rate of 40–50 mm/yr (Dewey et al., 1988; Dewey and Burke, 1973; Bilham et al., 1997). Since the initiation of continental-collision, continued shallow underthrusting of the Indian lithosphere beneath Eurasia (Nelson and the project

---

* Corresponding author.
E-mail address: mcnamara@usgs.gov (D.E. McNamara).

http://dx.doi.org/10.1016/j.tecto.2016.08.004

INDEPTH team, 1996; Makovsky and the project INDEPTH team, 1996; Makovsky et al., 1997; McNamara et al., 1997; Schulte-Pelkum et al., 2005; Nabelek et al., 2009; Caldwell et al., 2013) caused nearly 2500 km of crustal shortening resulting in the high elevations of the Himalaya mountain range (>5000 m), as well as the thickened crust (60–70 km) (Molnar, 1988) and eastward extrusion of the Tibetan Plateau lithosphere along major left-lateral strike-slip faults (Molnar and Tapponnier, 1975; Avouac and Tapponnier, 1993; McNamara et al., 1994) (Fig. 1).

In addition to spectacular topography, continental collision along the India-Eurasia plate boundary has produced numerous great earthquakes (M8+) throughout history (Bilham, 1995). Most recently, on 25 April 2015, the Mw 7.8 Gorkha earthquake ruptured a ~150 × 60 km section of the MHT that initiated beneath the Gorkha region of central Nepal at on a low-angle thrust fault dipping at 11° north that propagated eastward beneath Kathmandu (Hayes et al., 2015). This segment of the MHT has experienced several damaging earthquakes (1833, 1866, 1988) and is adjacent to segments to the northwest that ruptured in 1505 (Bilham, 1995) and to the southeast that ruptured in the 1934 Nepal-Bihar M8.1 earthquake (Fig. 1) (Sapkota et al., 2013).

1.2. Impact

The mainshock rupture was predominantly north of the capital city of Kathmandu, and caused very strong levels of shaking (MMI IX) resulting in hundreds of thousands of collapsed and damaged structures ($7 billion U.S. of economic losses) and loss of life (~8800 fatalities, 22,000 injuries) in Kathmandu and surrounding districts (Dixit et al., 2015). The shaking also caused significant loss of life through secondary hazards such as thousands of landslides in the steep-walled river and glacial valleys of the Himalaya (Collins and Jibson, 2015) and large (M6+) aftershocks at both ends of the mainshock rupture.

1.3. Aftershocks

Nearly 700 aftershocks were recorded on the Nepal Department of Mines and Geology (DMG) National Seismological Network (NSN) in the months following the Gorkha mainshock (Mw 7.3 2015-04-25 06:11:25 (UTC)) (Adhikari et al., 2015; Dixit et al., 2015; Hayes et al., 2015) with two of the largest aftershocks (mb 6.1 2015-04-25 06:15:22 (UTC), Mw 6.6 2015-04-25 06:45:21 (UTC)) within the first hour of the sequence, at either end of the mainshock rupture (Figs. 1 and 2). The second largest aftershock (Mw 6.7 2015-04-26 07:09:10.670 UTC) occurred one day later on the northeastern end of the rupture and 16 days later, in same region, the largest aftershock occurred (Mw 7.3 2015-05-12 07:05:19 (UTC)) (Figs. 1 and 2). In close proximity and within the same hour another large aftershock was registered (Mw 6.3 2015-05-12 07:36:54 (UTC)). The combined large aftershocks caused dozens of additional deaths and extensive damage to buildings in eastern Nepal.

Key issues of this earthquake sequence are the relatively high magnitude Mw 7.3 aftershock and the low magnitude-frequency distribution (b-value = 0.8) suggesting enrichment in large magnitude earthquakes relative to the global average (b-value = 1) (Adhikari et al., 2015).

1.4. Data instrumentation

Fig. 1 shows the distribution of local and regional seismic stations used to improve upon the U.S. Geological Survey (USGS) National Earthquake Information Center (NEIC) single-event hypocenters in the 2015 Mw 7.8 Gorkha, Nepal, earthquake sequence. In most cases, seismic phase picks were obtained from the Nepal DMG NSN and USGS NEIC combined catalog (COMCAT) earthquake catalogs. Phase picks were made on short-period seismic stations of the Nepal DMG NSN that are distributed regionally throughout Nepal (Adhikari et al., 2015), USGS strong-motion NetQuakes sensors that located in the Kathmandu Valley (Dixit et al., 2015) and additional global network broadband stations obtained from the USGS NEIC real-time earthquake processing system (Buland et al., 2009).

Additional seismic phase arrivals were manually picked on the local Nepal National Society for Earthquake Technology (NSET) N-SHAKE stations when available (Fig. 3a). In the weeks following the Mw 7.8 Gorkha earthquake, USGS scientists, supported by U.S. Agency for International Development (USAID) Office of Foreign Disaster assistance (OFDA), deployed to Nepal in order to install aftershock recording

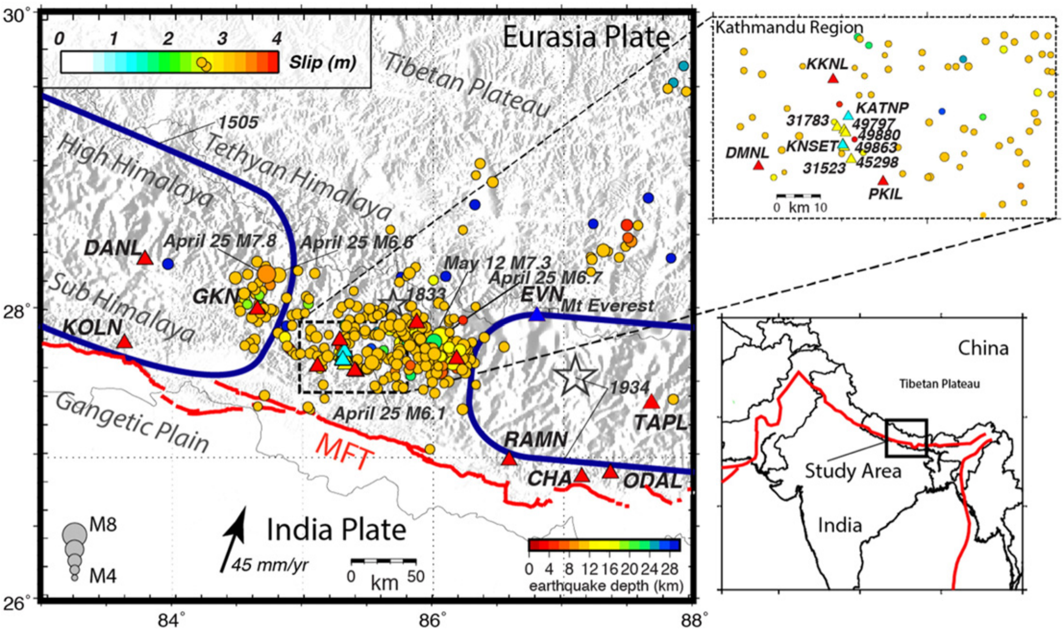

Fig. 1. Seismic station and regional tectonic map showing U. S. Geological Survey (USGS) National earthquake information center (NEIC) single-event epicenters as circles colored by depth. Nepal DMG NSN stations are shown as red triangles (Adhikari et al., 2015), U.S. Geological Survey NetQuakes sensors are shown as cyan triangles, global stations used by the USGS NEIC (IO.EVN) shown as a blue triangle, and N-SHAKE stations are shown as yellow triangles. Major plate boundaries and the MFT are shown as red lines (Berryman et al., 2014). Also shown are approximate epicenters (stars) and rupture areas (blue lines) for historic earthquakes in 1505, 1833 and 1934.

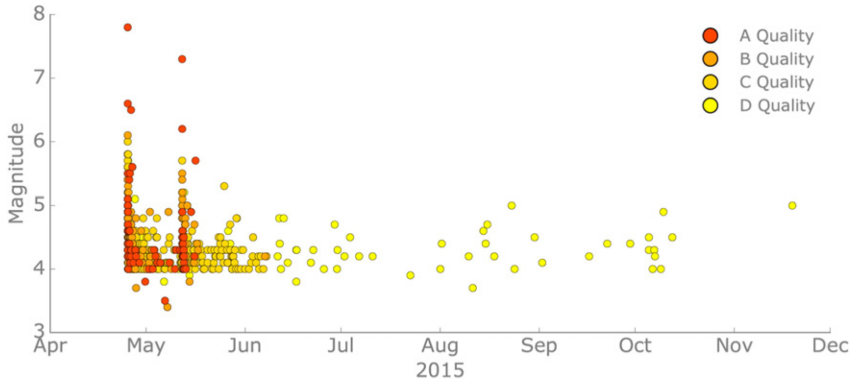

Fig. 2. Magnitude vs time for all 672 A, B, C, and D quality earthquakes. Two M > 6 aftershocks occurred within 1 h of the 25 April 2015 mainshock. Seventeen days after the mainshock on 12 May 2015 the largest Mw 7.3 aftershock occurred with a M > 6 aftershock within the same hour. Aftershocks have significantly decreased in magnitude and frequency since May 2015.

sensors and conduct a variety of damage and hazard assessment studies (Hough, 2015; Dixit et al., 2015; Collins and Jibson, 2015; Hayes et al., 2015; Moss et al., 2015). A significant accomplishment of the USAID OFDA deployment was improvement of the N-SHAKE network with distribution of additional Quake Catcher Network (QCN) (Cochran et al., 2009) micro-electro-mechanical system accelerometers in collaboration with Nepal NSET. In 2014, NSET installed a small number of QCN Onavi-B 16-bit instruments as a pilot study to test the feasibility of using low-cost strong-motion sensors to improve monitoring in the Kathmandu Valley of Nepal.

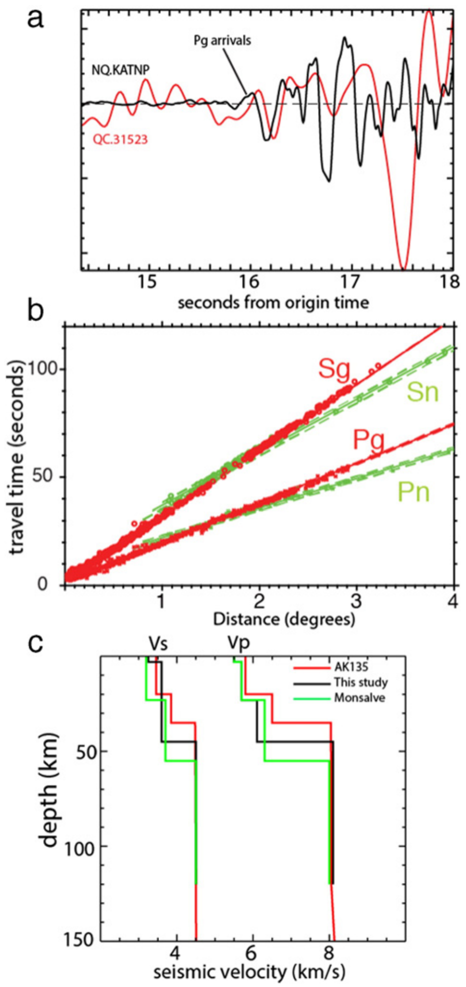

Fig. 3. (a) 2015 April 25 Mw 7.8 Pg arrivals recorded at N-SHAKE station QC.311523 and USGS Netquake station NQ.KATNP, roughly 70 km away from the epicenter in Kathmandu (Fig. 1). (b) Velocity model fit to the local and regional phases (Pg, Sg, Pn, Sn) travel times. (c) AK135 global model (red), Local velocity model determined in this study (black) and starting velocity model from Monsalve et al. (2008) (green).

In addition, a new sensor was installed at the USGS Netquakes station (NQ.KATNP) since it had not reported data in nearly two years. Triggers, including the Mw 7.8 mainshock, were recorded in the sensor memory and retrieved for manual arrival-time picking (Fig. 3a) and strong ground motion studies (Dixit et al., 2015). The older sensor was repaired and then installed at a new location (NQ.KNSET, Fig. 1) for use by the USGS NEIC real-time earthquake monitoring system.

2. Multiple-event relocation: Hypo-centroidal decomposition method

An initial catalog of Nepal DMG NSN and USGS NEIC single-event hypocenters and phase data were used as starting locations to determine calibrated multiple-event relocations using the Hypocentroidal Decomposition (HD). HD is a multiple-event procedure, first developed by Jordan and Sverdrup (1981), in the same class of methods that include Joint Hypocentral Determination (Douglas, 1967; Dewey, 1972) and Double Difference (Waldhauser and Ellsworth, 2000). HD is unique among these methods in having been developed for obtaining not only improved relative locations, but also calibrated absolute locations for an entire cluster of events, with reliable estimates of location uncertainty for each event.

The key feature of the HD algorithm is the decomposition. Decomposition greatly facilitates calibrated location studies through orthogonal projection operators of the multiple-event relocation problem into two independent inverse problems. These independent problems involve (1) the estimation of a set of cluster vectors that describe the location and origin time of each event with respect to a reference location of the hypocentroid that is defined as the geometrical mean of the current locations and origin times; and (2) inversion for an updated location and origin time for the hypocentroid in geographic coordinates, using the relative locations fixed by the cluster vectors and a subset of arrival-time data deemed most suitable for the problem. Separation of the problem in this way permits seismologically appropriate weighting for the two parts of the relocation process, which is critical for obtaining realistic uncertainties of the individual earthquake hypocentral parameters.

Arrival time data are weighted inversely to the uncertainty of the reading. Unlike other location algorithms, which use ad hoc values for data uncertainties for all samples of a given phase, we take advantage of the availability of repeated observations of the same phase at the same station for multiple events in a cluster and use the distribution of residuals from the observed arrival time data to estimate empirical arrival-time errors for each station-phase pair represented in the data set. These empirical arrival-time errors include traditional reading error, plus all other sources of variability in the residuals. Empirical arrival-time errors are estimated with a robust statistical method that minimizes the influence of outliers, and we then use the empirical errors to identify and eliminate outliers. This is an iterative process, followed at each step by relocation, repeated until the data set contains only arrivaltimes that are statistically consistent with the observed spread of residuals ($\pm 3\sigma$). Cluster vectors, that establish the relative location of each event with respect to the hypocentroid, are estimated using all available arrival time data, regardless of phase type or epicentral distance. This is possible because only travel time differences are used to estimate improved relative relocations, a common feature in all multiple-event relocation algorithms. Therefore, errors in the theoretical travel-time model used to calculate residuals and derivatives do not propagate significantly into relative location bias.

An important procedure for obtaining calibrated locations for a cluster of events in the HD method is to locate the hypocentroid of the cluster using only near-source data. This can be done in several ways (e.g., by reference to one or more events in the cluster for which very accurate locations are known independently), but for this study we used arrival time data at short epicentral distances. In this way we minimize the biasing effect of the imperfectly known velocity structure in the source region. It is especially important to avoid the use of Moho-refracted phases (*Pn*, *Sn*). Because of the relatively dense DMG NSN network, we avoided Moho-refracted phases by restricting the data set used for the hypocentroid to distances of less than about 60 km and still have a large number of direct crustal phase arrival times with broad azimuthal coverage.

An advantage of the HD method is its ability to relocate in an absolute sense the poorly constrained hypocenters by tying them to clusters of aftershocks that are recorded by the denser local network. One disadvantage of the HD method, in comparison with other methods of multiple-event relocation, is that computational effort grows rapidly with the number of events. To analyze the earthquake sequence of 672 events simultaneously would be impractical, so we divided the sequence into five sub-clusters based on station coverage and association with DMG NSN and USGS NEIC catalogs. Each sub-cluster was calibrated independently and contains events in all the main regions that were active during this sequence and overlap in space and time with the other two sub-clusters. Therefore, the five sub-clusters can be combined into a single seamless aftershock sequence. Sub-clusters were compared closely to ensure that there was no significant bias in location and depth between the five sub-clusters.

Additional improvement over the USGS NEIC and DMG NSN single-event hypocenters was achieved by developing a local velocity model. Starting with the southern 1D model of Monsalve et al. (2008) (Fig. 3) we forward modeled crust and mantle velocities to reduce the average travel-time residual for local and regional phase picks (Pg, Pn, Sg, Sn) (Fig. 3a) while simultaneously inverting for the highest quality hypocenters (Fig. 3b). The improved local velocity model (Fig. 3c, Table S3) significantly reduces the average travel time-residual relative to the AK135 global model (Kennett et al., 1995) used to determine USGS NEIC single-event hypocenters.

In summary, the HD relocation method provides improved hypocenter locations with minimized location bias and realistic estimates of location uncertainty for each earthquake. With local seismic stations available within two focal depths, location and depth uncertainty is improved significantly. In other cases uncertainty is greater and depths are often not changed from the original USGS NEIC or DMG NSN hypocenter. In addition, relocating earthquakes using HD can reduce, by a factor of 2, the scatter in hypocenter locations determined using single-event methods. Recent examples of HD applications and additional method details can be found in McNamara et al. (2014, 2015); and Hayes et al. (2013, 2014).

2.1. HD hypocenter quality, uncertainty and results

We determine relocated hypocenters for a total of 672 earthquakes in four different quality levels based on hypocenter uncertainty, seismic station coverage and association between the global USGS NEIC and local DMG NSN catalogs (Fig. 4, Table S1). We define 74 hypocenters as quality A that are located using global phase picks available to the USGS NEIC and local phase picks from the regional Nepal DMG NSN and NSET N-SHAKE stations located in Kathmandu (Table S2). For quality A events, origin times are associated within 5 s in both the DMG NSN (Adhikari et al., 2015) and USGS NEIC COMCAT catalogs (earthquake.usgs.gov). Quality A relocated hypocenters are within an epicentral distance of less than two focal depths to the nearest recording stations and in nine cases have USGS W-phase MTs for depth constraints. In general, quality A events have epicentral uncertainties <5 km and depth uncertainty <3 km (Figs. S1 and S2). Similar to quality A eents, 143 earthquakes are considered quality B were located using global stations, local and regional phase picks from Nepal DMG NSN and NSET N-SHAKE stations. The difference with quality A is that quality B hypocenters are less well constrained because epicentral distances are greater than two focal depths to the nearest recording stations. In general, quality B events have epicentral uncertainties 5–10 km and depth uncertainty 3–5 km (Figs. S1 and S2).

Hypocenters of 360 earthquakes were classified as quality C from 25 April to 07 June 2016 and were relocated with only Nepal DMG NSN station phase picks. In many cases quality C hypocenters are well constrained with hypocenter uncertainty <10 km (Figs. S1 and S2) however these events could not be associated, within a 5 s origin time difference, with any USGS NEIC COMCAT earthquakes. These earthquakes are generally smaller magnitude events that were not observed at distant regional and global stations.

Finally, 76 quality D earthquakes from 25 April 2015 to June 2016 were located with limited local USGS Netquakes and NSET N-SHAKE station phase picks and/or global networks available to the USGS NEIC (Figs. S1 and S2). No DMG NSN phase picks are available since the catalog is available only through in early November 2015 (Adhikari et al., 2015). Consequently, the closest global stations consistently available to the USGS NEIC are the strong motion USGS Netquakes (NQ.KATNP, NQ.KNSET) stations in Kathmandu and Global Seismograph Network (GSN) station IC.LSA, nearly 500 km away in southern Tibet. Hypocenters are improved slightly when station IO.EVN, located at Mt. Everest basecamp (Fig. 1), was available to the USGS NEIC for two weeks following the mainshock and when local travel-time picks were observed on NSET N-SHAKE stations in Kathmandu (Fig. 3a). On average, quality D events have epicentral and depth uncertainty greater than 10 to 20 km.

2.2. Constraints on hypocenter focal depth

In addition to application of the HD multiple-event relocation method, hypocenter depths determined in this study are improved over USGS NEIC single-event hypocenters because of the addition of local phase picks from the DMG NSN and NSET N-SHAKE stations (Fig. 3a), and DMG NSN single-event hypocenters due to the use of depth phases recorded on global network stations. Minimization of travel-time residuals for hypocenters with epicentral distances less than two focal depths was meticulously applied to constrain quality A depths. Quality B, C, and D hypocenters were determined by including well-constrained (quality A) hypocenters as constraints in the HD multiple-event inversion. The use of a local velocity model also contributes to improved focal depths (Table S3). HD relocated focal depths are on average shallower by ~5 km assuming the local versus global (AK135) velocity model (Kennett et al., 1995).

2.3. HD results compared to USGS NEIC and DMG NSN starting hypocenters

We did not locate all earthquakes observed at local seismic stations, but only those events for which there were a sufficient number of arrival-time observations and good azimuthal coverage to ensure a well-constrained hypocenter. Typically, smaller earthquakes ($M < 4.0$) were only recorded on a few local stations, making it difficult to determine location and depth accurately. In general, hypocenters shifted

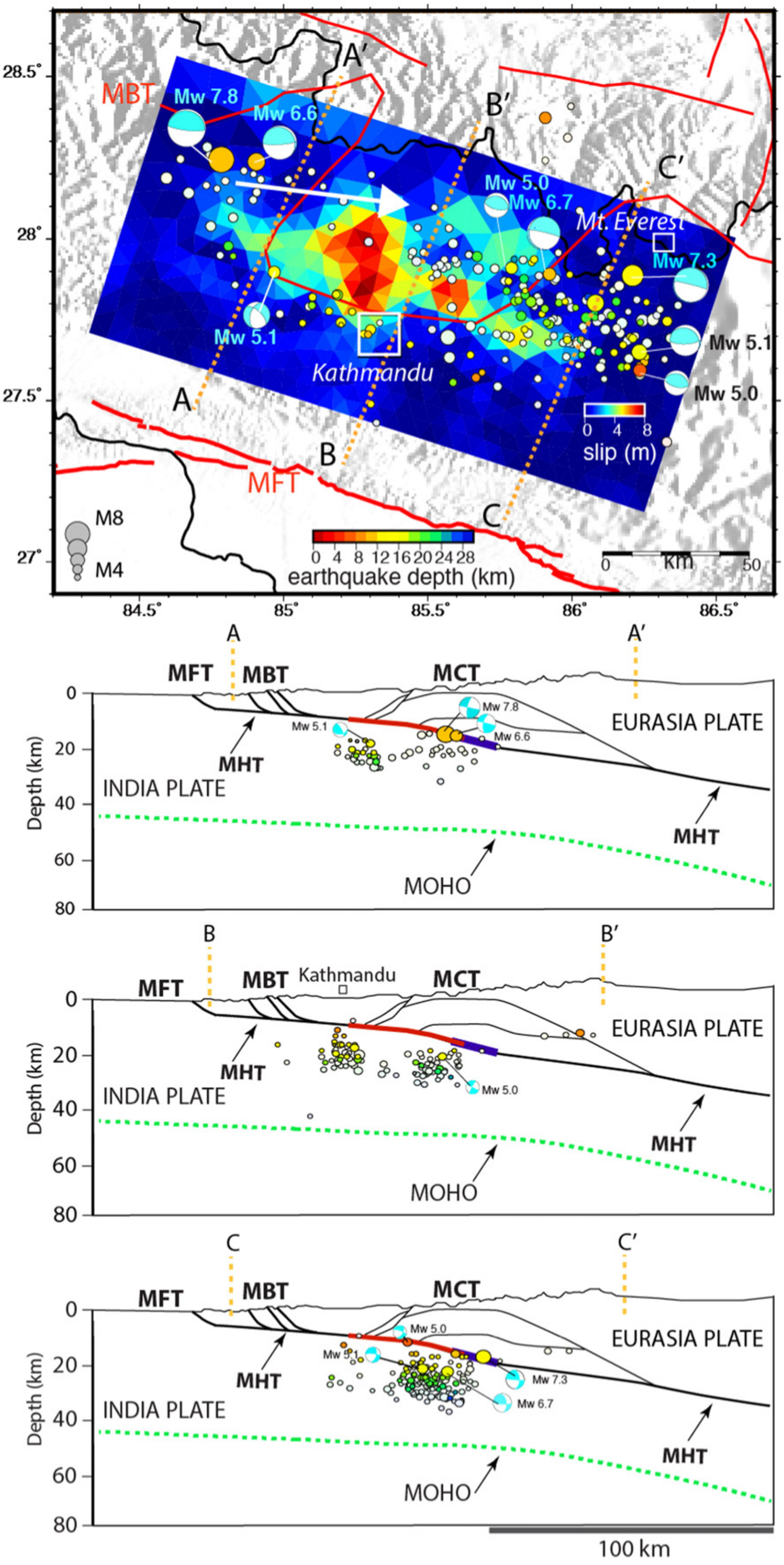

Fig. 4. Map showing 75 A and 217 B quality HD relocated hypocenters in profile and map view. A quality hypocenters shown as full color circles and B quality shown with 50% transparency, colored by depth. Blues lines show the location and extent of the cross-sections to the right. USGS NEIC W-phase moment tensor focal mechanisms shown in blue (Hayes et al., 2015). Also shown is the Mw7.8 mainshock median geodetic slip model drawn from 500 Monte Carlo simulations. The Gorkha rupture initiated in the west and propagated eastward (white arrow) with the region of maximum slip to the north of Kathmandu. Aftershocks are almost entirely absent in the regions of maximum slip and the MFT.

several kilometers from the USGS NEIC single-event solutions with uncertainty reduced by a factor of two for quality A, B and C events. For example, the mainshock epicenter has been relocated by approximately 10 km to the northeast (Fig. S1).

Fig. 4 shows a map of 217 quality A and B hypocenters along three cross-sections. HD relocated epicenters moved on average 10 to 15 km to the northeast relative to the USGS NEIC single-event epicenters (Fig. S1) and are distributed in a distinct NW to SE elongated ellipse to the north of Kathmandu. At the western end of the sequence (Fig. 4 A-A'), the Mw 7.8 (HD depth = 8.0 km, NEIC depth = 15 km, MT depth = 10 km) mainshock and Mw 6.6 (HD depth = 8.5 km, NEIC depth = 10 km, MT depth = 15 km) aftershocks are located at depths consistent with the MHT décollement (Lavé and Avouac, 2000). Smaller aftershocks occur on deeper structures forming a U shape to maximum depths of 25–30 km. Aftershocks in the central region of the sequence generally form two distinct northern and southern bands (Fig. 4 B-B′) that dip towards each other to depths of 30 km. The region to the east (Fig. 4 C-C′) contains the highest concentration of earthquakes and the largest Mw 7.3 and 6.7 aftershocks. The Mw 7.3 aftershock is located downdip of the Mw 7.8 mainshock at a depth along the MHT décollement defining the plate boundary (HD depth = 12 km, NEIC depth = 15 km, MT depth = 28 km). Aftershocks in the eastern region range in depth from 5 to 30 km and form a more shallow U shape than observed in profiles to the west.

HD relocated focal depths using a local velocity model tend to be more shallow than the NEIC single-event focal depths using the AK135 global model. HD relocated focal depths are also more shallow than the USGS W-phase MT due to use of the AK135 global velocity model and the difference in depth between the moment release versus the rupture initiation location (hypocenter).

2.4. Comparison with other studies

Fig. 5 shows comparisons with results from two recent studies by Nepal DMG NSN (Adhikari et al., 2015) and the Institute of Tibetan Plateau Research, Chinese Academy of Sciences (Bai et al., 2016). Our observations broadly agree with those of previous aftershock studies (Adhikari et al., 2015; Bai et al., 2016), although our catalog better resolves the earthquake depths and the absence of seismicity in the primary regions mainshock rupture due to use of a local velocity model and a combination of local and global phase picks.

Hypocenters determined in this study are on average 5 to 10 km deeper and move 5 to 15 km over a broad range of azimuths from the results of Adhikari et al., (2015). Hypocenters determined in this study are on average 5 to 15 km deeper and move 5 to 20 km in a narrow range of southwestern azimuths from the results of Bai et al., (2016). In addition, inclusion of local observations constrains aftershocks to greater depths as compared to earlier USGS NEIC investigations reliant primarily on regional and teleseismic data (Hayes et al., 2015).

Station coverage is considerably improved in our study over the Bai et al., (2016) study since the nearest stations are located over 500 km to the northeast of the Gorkha sequence in southern Tibet. Station coverage is also improved in our study over Adhikari et al., (2015) since hypocenters are not constrained with teleseismic arrivals (including depth-phases) recorded at stations in the global networks available to the USGS NEIC. We also removed significant outliers from the DMG NSN phase picks and developed a local velocity model that contributed to reduced travel-time residuals and hypocenter uncertainty (Fig. 3).

3. Geodetic slip model

In addition to improving aftershock locations, we mapped the spatial extent of finite fault slip from the April 25, 2015 Mw 7.8 Gorkha earthquake using a combination of space-based and in-situ geodetic observations. We analyzed four co-seismic interferometric synthetic aperture radar (InSAR) interferograms from the ALOS-2 L-band satellite and the Radarsat-2 C-band satellite (Hayes et al., 2015; Lindsay et al., 2015). These images spanned the time period February 2 to May 3, 2015, all prior to the May 12, 2015 Mw 7.3 aftershock. Both strip map and swath imaging modes were available from these sensors, and together they provided a complete image of the co-seismic displacement pattern, including the distinct subsidence and uplift lobes that are characteristic of a shallowly dipping thrust fault. We downsampled each interferogram to a computationally feasible number of observations (~10^3 observations from each interferogram) and estimated the noise covariance structure of the resampled interferograms (Lohman and Simons, 2005; Lohman and Barnhart, 2010). Line-of-sight radar observations of the mainshock were further supplemented by GPS observations from 15 continuous stations. We generated static offsets from daily GPS point position solutions processed by the University of Nevada Reno Geodetic Laboratory (see Data and Resources). Where available, we used time series spanning the period January 1, 2010 up to May 11, 2015 one day before the Mw 7.3 aftershock. Static co-seismic offsets and associated uncertainties for all three-displacement components were generated using the time series analysis methodology of Langbein (2004). This approach estimates both long-term displacement velocity and static displacement at a known earthquake origin time, and it accounts for temporally correlated noise in the GPS time series thus, providing a more realistic estimate of uncertainties that can be obtained through weighted least-squares fitting (e.g., Murray et al., 2014).

The finite fault slip distributions were generated following the general methodology of Barnhart et al. (2015). We first inverted the InSAR and GPS displacements for the best-fitting geometry and location of a single fault patch with uniform slip in a uniform elastic halfspace using the Neighbourhood Algorithm (Sambridge, 1999). The Neighbourhood Algorithm was allowed to search a broad model space, resulting in a best-fit fault geometry that dipped significantly steeper than the USGS W-phase solution (30°+ versus 11°). This discrepancy arises from the dominating effect of InSAR observations that primarily image vertical displacements and manifests as a tradeoff between inferred dip and depth of the fault plane. To address this, we fixed the dip of the fault plane to the USGS NEIC W-phase solution (Hayes et al., 2015) and allowed all other model

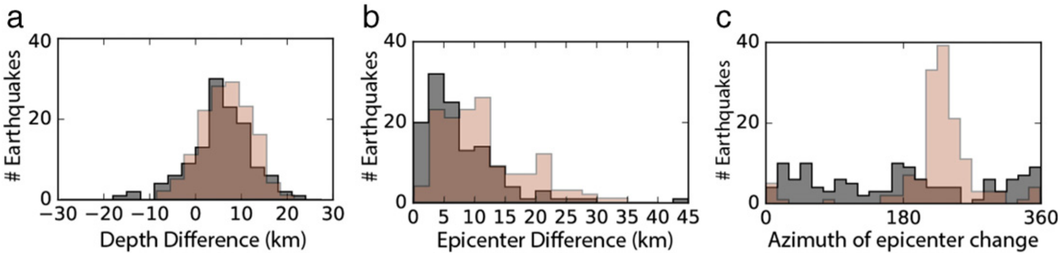

Fig. 5. A and B quality HD hypocenter comparisons to previous studies. a) Depth comparison. HD results from this study are generally 5–10 km deeper than Adhikari et al., (2015) (solid gray) and 5–15 km deeper than Bai et al., (2016) (transparent orange). b) Epicenter comparison. HD epicenters from this study moved by 5–15 km relative to Adhikari et al., (2015) (solid gray) and 5–20 km from Bai et al., (2016) (transparent orange). c) Epicenter change azimuth comparison. Change azimuths cover a broad range relative to epicenters from Adhikari et al., (2015) (solid gray) and are dominantly to the southwest of epicenters in Bai et al., (2016) (transparent orange).

parameters to vary freely. The best-fit model from this procedure (strike = 290°, dip = 7°) better approximates the orientation and depth of the W-phase solution. Furthermore, the RMS residual of this model for the InSAR observations is similar to more steeply dipping models (RMS difference of ~3 mm) where the dip and depth of the fault plane are allowed to vary freely, but the horizontal GPS displacements are fit much better. This demonstrates that a steeply dipping plane (>30°) is not required to explain the InSAR observations. Nonetheless, these tradeoffs highlight the difficulty of inferring the depth of a nearly horizontal fault plane from primarily vertical surface displacements and motivate the need for accurate fault plane geometries of subduction zones (e.g., Hayes et al., 2012).

We then fixed the best-fit single fault plane solution and extended the dimensions of the fault along-strike and down-dip. We applied an automated discretization approach that variably resamples the fault plane into heterogeneously sized triangles while simultaneously inverting for rake direction and finite slip in a homogeneous elastic halfspace (Barnhart and Lohman, 2010). The relative sizes of the triangular fault patches reflect the model resolution (larger patches indicate poor model resolution, while smaller patches indicate good model resolution) and introduce spatially varying regularization to the inverse problem (Fig. 4). The shallow dip of the responsible fault plane and the excellent coverage of InSAR observations allows for nearly uniform model resolution in our slip distribution. We imposed a minimum moment regularization and allowed the rake direction to vary freely in the thrust and strike-slip directions.

3.1. Geodetic slip model uncertainty

A common source of uncertainty in finite-fault slip distributions derived from InSAR is correlated atmospheric noise (e.g., Goldstein, 1995; Emardson et al., 2003; Lohman and Simons, 2005). To capture the biases introduced by this noise source in our slip distribution, we conduct a Monte Carlo error propagation analysis (Barnhart and Lohman, 2013). We add 500 realizations of synthetic noise to the predicted displacements of our best-fit slip distribution, where the synthetic noise has the same covariance structure as the resampled data. We then invert each synthetically noisy data set for fault slip using the same regularization and fault discretization described above. This procedure produces a population of fault-slip distributions that vary as a function of the noise in the observations. From this population, we extract the median, 16th, and 84th percentile slip distributions to highlight the possible range of slip distributions that fit the data (Figs. 6, S3 and S4).

3.2. Geodetic slip modeling results

Our slip distributions are broadly consistent with previous studies that utilized similar observations (Hayes et al., 2015; Zhang et al., 2015; Avouac et al., 2015; Galetzka et al., 2015; Wang and Fialko, 2015; Elliott et al., 2016). Slip propagated unilaterally to the east from the event epicenter, with the largest static slip values of up to ~8 m occurring immediately north of Kathmandu. Modeled slip distributions indicate a sharp up-dip cutoff of slip near 12.5 km with peak slip values at 15–16 km depth (Fig. 4). These depths are consistent with the W-phase MT depth of 15 km (Hayes et al., 2015), aftershock depth ranges found in this study, and slip depths reported by several other recent geodetic studies (e.g., Avouac et al., 2015; Galetzka et al., 2015; Elliott et al., 2016) but deeper depths proposed by Wang and Fialko (2015). The surface projection of slip cutoff is robust between all of these studies, demonstrating the distinct blind nature of this event and the lack of moment that was released within a ~45–50 km wide up-dip portion of the Main Frontal Thrust (MFT) south of Kathmandu. Additional to the up-dip seismic gap left by this earthquake, there are downdip regions of little to no slip that are well resolved by our observations northeast of Kathmandu (Fig. 4). One of these gaps was partially filled by the May 12, 2015 Mw 7.3 aftershock, as evidenced by other slip distributions generated from InSAR observations (Hayes et al., 2015; Lindsay et al., 2015).

4. Discussion: Implications for geodynamics and earthquake hazard

A combination of high-quality HD aftershock relocations and mainshock geodetic slip model allows us to further compare aftershock distribution to the rupture characteristics of the Mw 7.8 and Mw 7.3 earthquakes. The earthquake sequence was most active in the west and east with aftershocks generally surrounding the region of major slip (>4 m) during the Mw 7.8 mainshock (Fig. 4). The highest densities of earthquakes occur ENE of the mainshock rupture in regions of minimum slip, and along the up-dip and down-dip edges of the mainshock rupture zone in regions of positive Coulomb failure stress change (ΔCFS) (Li et al., 2017-in this issue; Hayes et al., 2015). The absence of aftershocks, along up-dip segments of the mainshock maximum slip region, is consistent with a deficit of post-event slip (Mencin et al., 2016).

At depth, aftershocks are also likely occurring on activated structures beneath the mainshock rupture in deeper regions of positive ΔCFS (Stein, 1999). The high density of aftershocks ENE of the mainshock rupture occur updip from the Mw 7.3 aftershock. Few aftershocks located within 50 km of the MFT surface trace, which in congruence with our fault-rupture model, suggests that this portion of the plate interface did not slip during the Mw 7.8 mainshock.

Fig. 7 is a generalized cross section of the Himalayan thrust system (after Lavé and Avouac (2000) and Kumar et al., (2006)) through Kathmandu, showing major faults (Main Frontal Thrust (MFT), Main Himalayan Thrust (MHT), Main Boundary Thrust (MBT), Main Central Thrust (MCT)) and the distribution of aftershocks in cross-section. Also shown are interpreted receiver function common conversion point (CCP) stacks from Schulte-Pelkum et al. (2005) showing P-wave

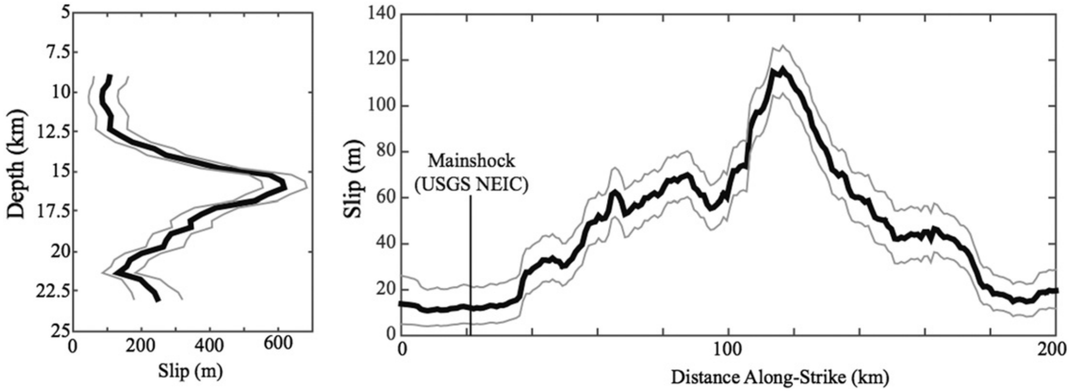

Fig. 6. Mainshock slip versus depth (left) and along strike (right). The black profile reflects the median slip distribution drawn from 500 Monte Carlo simulations (Fig. 5), and the gray profiles reflect the 16th and 84th percentiles of inferred slip, respectively.

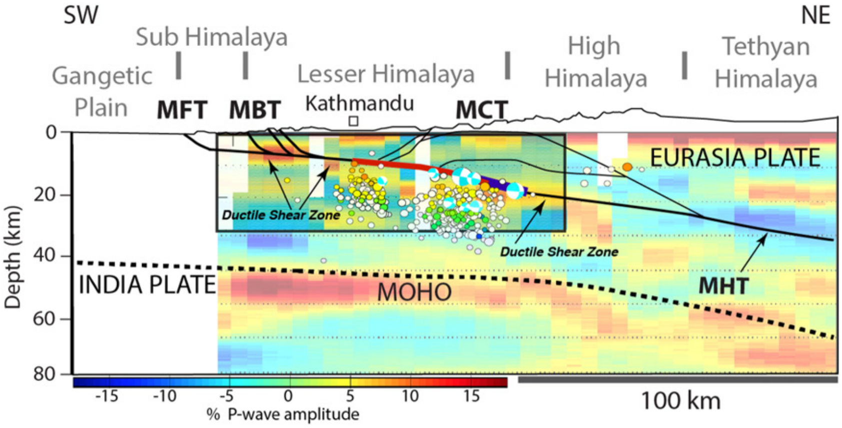

Fig. 7. Generalized cross section of the Himalayan thrust system through Kathmandu with calibrated aftershock relocations (A quality are light gray circles, B quality shown with 50% transparency) and major faults (black lines) after Lavé and Avouac (2000) and Kumar et al., (2006) (MFT, Main Frontal thrust; MBT, Main Boundary thrust; MCT, Main Central thrust; and MHT, Main Himalayan thrust). Approximate ruptures for the Mw 7.8 mainshock (gray line) and Mw 7.3 aftershock (dark gray line) shown along the MHT. Relocated aftershocks surround the region of maximum mainshock slip in cross-section as well as map view, and are primarily located at a depth that corresponds to the shear zone (red and blue lines) and near the boundary between the upper and lower crust imaged by Schulte-Pelkum et al., (2005) using CCP north-south receiver function component difference stacks (black box inset). Color scale is stacked radial receiver function amplitude expressed as a percentage of the direct P arrival. Also shown are the CCP stack-interpreted boundary between the upper and lower Indian crust (thin dashed black line) and the Moho (thick dashed black line). USGS NEIC W-phase moment tensor focal mechanisms shown in profile in light blue (Hayes et al., 2015).

receiver function amplitudes which are interpreted as the major geologic interfaces in the India-Eurasia continental collision zone and a seismically anisotropic shear-zone along the MHT.

In general most aftershocks occur within or below the MHT decollement in a 10–15 km thick depth interval of low-angle reverse faulting (Fig. 7). Given the similarity in orientation of the focal mechanisms between mainshock and aftershocks, and the coincident location of the aftershock seismicity with a shear zone previously imaged using receiver functions (Schulte-Pelkum et al., 2005), we interpret this region of aftershock activity as a subduction channel where shear deformation occurs within unconsolidated, high pore fluid pressure, viscous material sandwiched between stronger upper Eurasian and underthrusting lower Indian tectonic plates (Vannucchi et al., 2012). A subduction channel in a continental collision zone can be particularly well developed and thickened due to the large amounts of sediments contributed from two continental plates and stress and fluid pressure is anomalously high due to the rapid convergence rate in the Eurasia-India continental collision (45 mm/yr) (von Huene and Scholl, 1991).

Some field studies of exhumed fossil subduction zones support the model of a several kilometer thick zone with seismic ruptures within the channel that cross-cut foliation developed within the channel (Bachmann et al., 2009; Dielforder et al., 2015; Fagereng, 2011; Angiboust et al., 2015), while others argue for strain localization with mélange fabric ascribed to other deformational processes (Wakabayashi and Rowe, 2015; Raymond and Bero, 2015; Platt, 2015); the field studies are usually from ocean-continent collision zones, with differences in the Himalayan continent-continent collision possible or likely. At the depth where the Gorkha aftershocks occur, the subduction channel is strong enough to support earthquakes. Foliation developed in the shallow zone of seismogenesis (Vannucchi et al., 2012; Bachmann et al., 2009) may be parallel to the MHT where strain is localized, but may also show high angles to the MHT, matching the anisotropy observed in receiver functions. Receiver functions are inherently more sensitive to dipping foliation than subhorizontal foliation (Schulte-Pelkum and Mahan, 2014); hence the steeper foliation inferred from receiver functions (Schulte-Pelkum et al., 2005) does not preclude additional MHT-parallel fabric. An MHT-parallel foliation is consistent with W-phase moment tensor shallow focal planes determined for the largest earthquakes in the sequence (Hayes et al., 2015). Farther down-dip the subduction channel is deforming by ductile shear and has no observed aftershocks. Up-dip at depths of 0 to 10 km, where the subduction-channel overlaps the MBT and MFT, we observe very few aftershocks and no mainshock slip in a region of positive increase in CFS (Hayes et al., 2015).

4.1. Implications for earthquake hazard

The Gorkha earthquake sequence aftershocks occur in low-slip regions surrounding the maximum slip of the mainshock fault model (Figs 4 and 7). The “locked” updip segment of the MFT and downdip “creeping” ductile-shear segment of the MHT are in a region with no aftershocks, no mainshock slip and positive ΔCFS increase (Li et al., 2017-in this issue; Hayes et al., 2015). Positive ΔCFS magnitudes of as little as 0.1 bar (0.01 MPa) have been shown to be sufficient to encourage the occurrence of future earthquakes in regions where faults are critically stressed and close to failure (Stein, 1999). Up-dip segments of the MHT should be considered high hazard for future damaging earthquakes.

All of the M6–7 aftershocks occurred in regions with positive ΔCFS increases and strongly shaken by the Mw 7.8 mainshock. When significant aftershocks occur in regions that received strong shaking during the mainshock, earthquake hazard is increased due to already damaged and vulnerable structures. The largest M6–7 aftershocks occurred in the western and eastern ends of the sequence that experienced strong to severe shaking intensity during the Mw 7.8 mainshock. Several dozen people were killed as a result of the collapse of vulnerable buildings during the Mw 7.3 aftershock.

The Mw 7.8 2015 Gorkha earthquake is a relatively small event in the seismic cycle of the Himalaya. Much higher magnitude earthquakes have occurred throughout geologic history as interseismic strain accumulates (Pandey et al., 1995) along the rapidly converging Indian-Eurasian continental collision boundary (20 mm/yr of convergence across the Himalaya (Stevens and Avouac (2015)). For example, the 2015 Mw 7.8 Gorkha earthquake sequence is bounded by larger magnitude earthquakes to the west in 1505 and the east in 1934 (Hayes et al., 2015) (Fig. 1). It is possible that the 2015 and 1833 events near Kathmandu were smaller than the events to the west (1505) and east (1934) because lateral differences in the wedge structure inhibited rupture to shallow depths. This has been suggested to account for the spatial distribution of earthquake magnitude along the Chilean subduction zone (Contreras-Reyes et al., 2010). Analysis of wedge structure using the available stations along the Lesser Himalaya will enable this question to be addressed.

5. Conclusions

This work is a multi-disciplinary effort to understand the Mw 7.8 Gorkha earthquake in the context of tectonic evolution of the Himalaya and associated seismic hazards. Seismic phase picks from several sources are used construct a comprehensive catalog of calibrated hypocenters of the Gorkha earthquake sequence. A geodetic slip model for the Mw 7.8 Gorkha earthquake demonstrating that it ruptured a ~150 km × 60 km patch of the MHT over an area surrounding but predominantly north of the capital city of Kathmandu. The distribution of aftershock seismicity surrounds the mainshock maximum slip patch and is generally limited to 10–15 km thick shallowly dipping zone at or below the MHT décollement with depths generally increasing to the north beneath the higher Himalaya. The largest Mw 7.3 aftershock and the highest concentration of aftershocks occurred east of the mainshock rupture, on a segment of the MHT décollement that was positively stressed towards failure (Hayes et al., 2015). We find that the near-surface portion of the MHT, south of Kathmandu, is primarily absent of aftershocks and slip during the mainshock. Results from this study characterize the details of the Gorkha earthquake sequence and provide constraints on where earthquake hazard remains high. Segments of the MHT, up-dip of the 2015 Gorkha rupture, likely have high hazard for future damaging earthquakes in this densely populated and vulnerable region.

6. Data and resources

Quake Catcher Network (http://qcn.caltech.edu/).

USGS NEIC COMCAT http://earthquake.usgs.gov

USGS event pages an be found here:

Mw7.8 http://earthquake.usgs.gov/earthquakes/eventpage/us20002926#general_region

Mw7.3 http://earthquake.usgs.gov/earthquakes/eventpage/us20002ejl#general_region

USGS Netquakes http://earthquake.usgs.gov/monitoring/netquakes/

USGS GSN http://earthquake.usgs.gov/monitoring/gsn/

Nepal DMG NSN http://www.seismonepal.gov.np/index.php?linkId=58

Nepal NSET http://www.nset.org.np/nset2012/

USAID OFDA https://www.usaid.gov/who-we-are/organization/bureaus/bureau-democracy-conflict-and-humanitarian-assistance/office-us

InSAR URL: University of Nevada-Reno Geodetic Laboratory (http://geodesy.unr.edu

Acknowledgements

We thank analysts at the Nepal DMG NSN and USGS NEIC for phase picks used in this study. We thank S. Hough for leading the USGS/USAID field team and J. Galetzka (UNAVCO) for help reviving station NQ.KATNP. We thank the staff of NSET for hosting the seismic team and installation and implementation of the stations in the N-SHAKE network. We thank the QCN project for providing the MEMs sensors and making data available on their website. Valuable insights on logistics and data interpretation were provided by G.P. Hayes, R.W. Briggs, E. Cochran (USGS). Remote Netquake QC was provided by J. Luetgert and L. Gee. We thank staff at Nepal NSET for their hard work and guidance in Nepal, Surya Shrestha, Dev Maharjan, San Jev, Susan Adhikari, Bijendra.

We thank staff at the Nepal DMG NSN for their dedication and valuable data, including S. Sapkota. This research was supported by the United States Geological Survey's National Earthquake Hazards Reduction Program. Tectonophysics and USGS reviewers provided thoughtful comments that improved this manuscript. Any use of trade, product, or firm names is for descriptive purposes only and does not imply endorsement by the U.S. Government.

Appendix A. Supplementary data

Supplementary data associated with this article can be found in the online version, at http://dx.doi.org/10.1016/j.tecto.2016.08.004. These data include the Google map of the most important areas described in this article.

References

Adhikari, L.B., Gautam, U.P., Koirala, B.P., Bhattarai, M., Kandel, T., Gupta, R.M., Timsina, C., Maharjan, N., Maharjan, K., Dahal, T., Hoste-Colomer, R., Cano, Y., Dandine, M., Guilhem, A., Merrer, S., Roudil, P., Bollinger, L., 2015. The aftershock sequence of the 2015 April 25 Gorkha–Nepal earthquake. Geophys. J. Int. 203 (3), 2119–2124. http://dx.doi.org/10.1093/gji/ggv412.

Angiboust, S., Kirsch, J., Oncken, O., Glodny, J., Monie, P., Rybacki, E., 2015. Probing the transition between seismically coupled and decoupled segments along an ancient subduction interface. Geochem. Geophys. Geosyst. 16, 1905–1922. http://dx.doi.org/10.1002/2015GC005776.

Avouac, J.P., Tapponnier, P., 1993. Kinematic model of active deformation in central Asia. Geophys. Res. Lett. 20, 895–898.

Avouac, J.-P., Meng, L., Wei, S., Wang, T., Ampuero, J.-P., 2015. Lower edge of locked Mian Himalayan Thrust unzipped by the 2015 Gorkha earthquake. Nat. Geosci. 8, 708–711. http://dx.doi.org/10.1038/ngeo2518.

Bachmann, R., Oncken, O., Glodny, J., Seifert, W., Georgieva, V., Sudo, M., 2009. Exposed plate interface in the European Alps reveals fabric styles and gradients related to an ancient seismogenic coupling zone. J. Geophys. Res. 114, B05402. http://dx.doi.org/10.1029/2008JB005927.

Bai, L., Liu, H., Ritsema, J., Mori, J., Zhang, T., Ishikawa, Y., Li, G., 2016. Faulting structure above the Main Himalayan Thrust as shown by relocated aftershocks of the 2015 MW7.8 Gorkha, Nepal earthquake. Geophys. Res. Lett. 43. http://dx.doi.org/10.1002/2015GL066473.

Barnhart, W.D., Lohman, R.B., 2010. Automated fault model discretization for inversions for coseismic slip distributions. J. Geophys. Res. Solid Earth 115 (B10). http://dx.doi.org/10.1029/2010JB007545 n/a–n/a.

Barnhart, W.D., Lohman, R.B., 2013. Phantom earthquakes and triggered aseismic creep: vertical partitioning of strain during earthquake sequences in Iran. Geophys. Res. Lett. 40 (5), 819–823. http://dx.doi.org/10.1002/grl.50201.

Barnhart, W.D., Murray, J.R., Yun, S.-H., Svarc, J.L., Samsonov, S.V., Fielding, E.J., Brooks, B.A., Milillo, P., 2015. Geodetic constraints on the 2014 M 6.0 South Napa earthquake. Seismol. Res. Lett. 86 (2 A), 335–343. http://dx.doi.org/10.1785/0220140210.

Berryman, K., Ries, W., Litchfield, N., 2014. The Himalayan Frontal thrust: attributes for seismic hazard version 1.0, December 2014, GEM Faulted Earth project. available from http://www.nexus.globalquakemodel.org/ last accessed October 2015.

Bilham, R., 1995. Location and magnitude of the 1833 Nepal earthquake and its relation to the rupture zones of contiguous great Himalayan earthquakes. Curr. Sci. 69, 101–127.

Bilham, R., Larson, K., Freymuller, J., 1997. GPS measurements of present-day convergence across the Nepal Himalaya. Nature 386, 61–64.

Buland, R.P., Guy, M., Kragness, D., Patton, J., Erickson, B., Morrison, M., Bryan, C., Ketchum, D., Benz, H., 2009. Comprehensive Seismic Monitoring for Emergency Response and Hazards Assessment: Recent Developments at the USGS National Earthquake Information Center, American Geophysical Union, Fall Meeting 14–18 Dec. 2009, Abstract #S11B–1696.

Caldwell, W.B., Klemperer, S.L., Lawrence, J., Rai, S.S., Ashish, 2013. Characterizing the Main Himalayan Thrust in the Garhwal Himalaya, India with receiver function CCP stacking. EPSL 367, 15–27. http://dx.doi.org/10.1016/j.epsl.2013.02.009.

Cochran, E.S., Lawrence, J.F., Christensen, C., Jakka, R.S., 2009. The Quake-Catcher Network: citizen science expanding seismic horizons. Seismol. Res. Lett. 80, 26–30. http://dx.doi.org/10.1785/gssrl.80.1.26.

Collins, B.D., Jibson, R.W., 2015. Assessment of existing and potential landslide hazards resulting from the April 25, 2015 Gorkha, Nepal earthquake sequence. U.S. Geol. Surv. Open- File Rept. 2015–1142 http://dx.doi.org/10.3133/ofr20151142 50 pp.

Contreras-Reyes, E., Flueh, E.R., Grevemeyer, I., 2010. Tectonic control on sediment accretion and subduction off south central Chile: implications for coseismic rupture processes of the 1960 and 2010 megathrust earthquakes. Tectonics 29, TC6018. http://dx.doi.org/10.1029/2010TC002734 2010.

Dewey, J.W., 1972. Seismicity & tectonics of Western Venezuela. Bull. Seismol. Soc. Am. 2, 1711–1751.

Dewey, J.F., Burke, K.C.A., 1973. Tibetan Variscan, and Precambrian basement reactivation: products of continental collision. J. Geol. 81, 683–692.

Dewey, J.F., Shackleton, R.M., Cheng, F.R.S.C., Yiyin, S., 1988. The tectonic evolution of the Tibetan Plateau. Philos. Trans. R. Soc. Lond. 327, 379–413.

Dielforder, A., Vollstaedt, H., Vennemann, T., Berger, A., Herwegh, M., 2015. Linking megathrust earthquakes to brittle deformation in a fossil accretionary complex. Nat. Commun. 6, 7504. http://dx.doi.org/10.1038/ncomms8504.

Dixit, M.A., Shrestha, S.N., Rajaure, S., Ringler, A., Sumy, D.F., Cochran, E., Hough, S.E., Martin, S.S., Gibbons, S., Luetgert, J.H., Galetzka, J., McNamara, D.E., 2015. Strong motion observations of the M7.8 Gorkha, Nepal earthquake sequence and development of the N-SHAKE strong motion network. Seismol. Res. Lett. 86 (6), 1533–1539. http://dx.doi.org/10.1785/doi:0220150146.

Douglas, A., 1967. Joint epicenter determination. Nature 215 (5096), 47–48.

Elliott, J.R., Jolivet, R., González, P.J., Avouac, J.-P., Hollingsworth, J., Searle, M.P., Stevens, V.L., 2016. Himalayan megathrust geometry and relation to topography revealed by the Gorkha earthquake. Nat. Geosci. http://dx.doi.org/10.1038/ngeo2623 advance online publication.

Emardson, T.R., Simons, M., Webb, F.H., 2003. Neutral atmospheric delay in interferometric synthetic aperture radar applications: statistical description and mitigation. J. Geophys. Res. Solid Earth 108 (B5). http://dx.doi.org/10.1029/2002JB001781 n/a–n/a.

Fagereng, A., 2011. Geology of the seismogenic subduction thrust interface. In: Fagereng, A., Toy, V.G., Rowland, J.V. (Eds.), Geology of the Earthquake Source: A Volume in Honour of Rick Sibson. Geological Society, London, Special Publications Vol. 359, pp. 55–76. http://dx.doi.org/10.1144/SP359.4.

Galetzka, J., et al., 2015. Slip pulse and resonance of the Kathmandu basin during the 2015 Gorkha earthquake, Nepal. Science 349 (6252), 1091–1095. http://dx.doi.org/10.1126/science.aac6383.

Goldstein, R., 1995. Atmospheric limitations to repeat-track radar interferometry. Geophys. Res. Lett. 22 (18), 2517–2520. http://dx.doi.org/10.1029/95GL02475.

Hayes, G.P., Wald, D.J., Johnson, R.L., 2012. Slab1.0: a three-dimensional model of global subduction zone geometries. J. Geophys. Res. Solid Earth 117 (B1). http://dx.doi.org/10.1029/2011JB008524 n/a–n/a.

Hayes, G.P., Bergman, E., Johnson, K., Benz, H., Brown, L., Melzer, A., 2013. Seismotectonic framework of the February 27, 2010 Mw 8.8 Maule, Chile earthquake sequence. Geophys. J. Int. 195, 1034–1051. http://dx.doi.org/10.1093/gji/ggt238.

Hayes, G.P., Herman, M.W., Barnhart, W.D., Furlong, K.P., Riquelme, S., Benz, H., Bergman, E., Barrientos, S., Earle, P.S., Samsonov, S., 2014. Continuing megathrust earthquake potential in Chile after the 2014 Iquique earthquake. Nature 512 (7514), 295–298.

Hayes, G.P., Barnhart, W., Briggs, R., Yeck, W., McNamara, D.E., Wald, D., Nealy, J., Benz, H., Gold, R., Jaiswal, K., Marano, K., Earle, P., Hearne, M., Smoczyk, G., Wald, L., Samsonov, S., 2015. Rapid characterization of the 2015 Mw 7.8 Nepal (Gorkha) earthquake. Seismol. Res. Lett. 86 (6), 1557-156. http://dx.doi.org/10.1785/0220150145.

Hough, S., 2015. Introduction to the focus section on the 2015 Gorkha, Nepal, earthquake. Seismol. Res. Lett. 86 (6). http://dx.doi.org/10.1785/0220150138.

Jordan, T.H., Sverdrup, K.A., 1981. Teleseismic location techniques and their application to earthquake clusters in the south-central Pacific. Bull. Seismol. Soc. Am. 71, 1105–1130.

Kennett, B.L.N., Engdahl, E.R., Buland, R., 1995. Constraints on seismic velocities in the earth from travel times. Geophys. J. Int. 122, 108–124.

Kumar, S., Wesnousky, S.G., Rockwell, T.K., Briggs, R.W., Thakur, V.C., Jayangondaperumal, R., 2006. Paleoseismic evidence of great surface rupture earthquakes along the Indian Himalaya. J. Geophys. Res. 111 (B03304). http://dx.doi.org/10.1029/2004JB003309.

Langbein, J., 2004. Noise in two-color electronic distance meter measurements revisited. J. Geophys. Res. Solid Earth 109 (B4), B04406. http://dx.doi.org/10.1029/2003JB002819.

Lavé, J., Avouac, J.P., 2000. Active folding of fluvial terraces across the Siwalik Hills, Himalaya of central Nepal. J. Geophys. Res. 105, 5735–5770.

Li, L., Ya, D., Meng, X., Peng, Z., Wang, B., 2017. Increasing seismicity in Southern Tibet following the 2015 Mw7.8 Gorkha, Nepal earthquake. Tectonophysics 714-715, 62–70 (in this issue).

Lindsay, E., Natsuaki, R., Xu, X., Shimada, M., Hashimoto, H., Melgar, D., Sandwell, D.T., 2015. Line of sight deformation from ALOS-2 interferometry: Mw 7.8 Gorkha earthquake and Mw 7.3 aftershock. Geophys. Res. Lett. 42 (16), 6655–6661.

Lohman, R.B., Barnhart, W.D., 2010. Evaluation of earthquake triggering during the 2005–2008 earthquake sequence on Qeshm Island, Iran. J. Geophys. Res. Solid Earth 115, 12413. http://dx.doi.org/10.1029/2010JB007710.

Lohman, R.B., Simons, M., 2005. Some thoughts on the use of InSAR data to constrain models of surface deformation: noise structure and data downsampling. Geochem. Geophys. Geosyst. 6 (1). http://dx.doi.org/10.1029/2004GC000841 n/a–n/a.

Makovsky, Y., the project INDEPTH team, 1996. Structural elements of the Southern Tethyan Himalaya crust from wide-angle seismic data. Tectonics 15, 997–1005.

Makovsky, Y., Klemperer, S.L., Rathschbacher, L., Brown, L.D., Li, M., Zhao, W., Meng, F., 1997. INDEPTH wide-angle reflection observation of P-wave-to-S-wave conversion from crustal bright spots in Tibet. Science 274, 1690–1691.

McNamara, D.E., Owens, T.J., Silver, P.G., Wu, F.T., 1994. Shear wave anisotropy beneath the Tibetan Plateau. J. Geophys. Res. 99, 13,655–13,665.

McNamara, D.E., Walter, W.R., Owens, T.J., Ammon, C.J., 1997. Upper mantle velocity structure beneath the Tibetan plateau from Pn travel time tomography. J. Geophys. Res. 102, 493–505.

McNamara, D.E., Benz, H.M., Herrmann, R.B., Bergman, E.A., Chapman, M., 2014. The M_w 5.8 Central Virginia seismic zone earthquake sequence of August 23, 2011: constraints on earthquake source parameters and fault geometry. Bull. Seismol. Soc. Am. 104, 1.

McNamara, D.E., Benz, H.M., Herrmann, R.B., Bergman, E.A., Earle, P., Holland, A., Baldwin, R., Gassner, A., 2015. Earthquake hypocenters and focal mechanisms in central Oklahoma reveal a complex system of reactivated subsurface strike-slip faulting. Geophys. Res. Lett. 42, 2742–2749. http://dx.doi.org/10.1002/2014GL062730.

Mencin, D., Bendick, R., Upreti, B.N., Adhikari, D.P., Gajurel, A.P., Bhattarai, R.R., Shrestha, H.R., Bhattarai, T.N., Manandhar, N., Galetzka, J., Knappe, E., Pratt-Sitaula, B., Aoudia, A., Bilham, R., 2016. Himalayan strain reservoir inferred from limited afterslip following the Gorkha earthquake. Nat. Geosci. http://dx.doi.org/10.1038/ngeo2734.

Molnar, P., 1988. A review of geophysical constraints on the deep structure of the Tibetan Plateau, the Himalaya and the Karakoram, and their tectonic implications. Trans. R. Soc. Lond. Ser. A 327, 33–88.

Molnar, P., Tapponnier, P., 1975. Cenozoic tectonics of Asia; effects of a continental collision. Science 189 (4201), 419–426. http://dx.doi.org/10.1126/science.189.4201.419.

Monsalve, G., Sheehan, A., Rowe, C., Rajaure, S., 2008. Seismic structure of the crust and the upper mantle beneath the Himalayas: evidence for eclogitization of lower crustal rocks in the Indian plate. J. Geophys. Res. 113 (B08315). http://dx.doi.org/10.1029/2007JB005424.

Moss, R.E.S., Thompson, E.M., Kieffer, D.S., Tiwari, B., Hashash, Y.M.A., Acharya, I., Adhikari, B., Asimaki, D., Clahan, K.B., Collins, B.D., 2015. Geotechnical effects of the 2015 Mw 7.8 Gorkha, Nepal, earthquake and aftershocks. Seismol. Res. Lett. 86 (6). http://dx.doi.org/10.1785/0220150158.

Murray, J.R., Minson, S.E., Svarc, J.L., 2014. Slip rates and spatially variable creep on faults of the northern San Andreas system inferred through Bayesian inversion of global positioning system data. J. Geophys. Res. Solid Earth 119 (7), 2014JB010966. http://dx.doi.org/10.1002/2014JB010966.

Nabelek, J., Hetenyi, G., Vergne, J., Sapkota, S., Kafle, B., Jiang, M., Su, H., Chen, J., Huang, B., 2009. The Hi-CLIMB Team, 2009. Underplating in the Himalaya–Tibet collision zone revealed by the Hi-CLIMB experiment. Science 325 (September (5946)), 1371–1374 URL/http://www.sciencemag.org/cgi/content/abstract/325/5946/1371S.

Nelson, K.D., the project INDEPTH team, 1996. Partially molten middle crust beneath southern Tibet: synthesis of project INDEPTH results. Science 274, 1684–1687.

Pandey, M.R., Tandukar, R.P., Avouac, J.-P., Lave, J., Massot, J.-P., 1995. Interseismic strain accumulation on the Himalayan crustal ramp (Nepal). Geophys. Res. Lett. 22, 751–754.

Platt, J.P., 2015. Origin of Franciscan blueschist-bearing melange at San Simeon, central California coast. Int. Geol. Rev. 57 (5–8), 843–853. http://dx.doi.org/10.1080/00206814.2014.902756.

Raymond, L.A., Bero, D.A., 2015. Sandstone-matrix mélanges, architectural subdivision, and geologic history of accretionary complexes: a sedimentological and structural perspective from the Franciscan Complex of Sonoma and Marin counties, California, USA. Geosphere 11 (4), 1077–1110. http://dx.doi.org/10.1130/GES01137.1.

Sambridge, M., 1999. Geophysical inversion with a neighbourhood algorithm—I. Searching a parameter space. Geophys. J. Int. 138 (2), 479–494. http://dx.doi.org/10.1046/j.1365-246X.1999.00876.x.

Sapkota, S., Bollinger, L., Klinger, Y., Tapponnier, P., Gaudemer, Y., Tiwari, D., 2013. Primary surface ruptures of the great Himalayan earthquakes in 1934 and 1255. Nat. Geosci. 6, 71–76. http://dx.doi.org/10.1038/ngeo1669.

Schulte-Pelkum, V., Mahan, K., 2014. A method for mapping crustal deformation and anisotropy with receiver functions and first results from USArray, Earth planet. Sci. Lett. 402, 221–233. http://dx.doi.org/10.1016/j.epsl.2014.01.050.

Schulte-Pelkum, V., Monsalve, G., Sheehan, A., Pandey, M.R., Sapkota, S., Bilham, R., Wu, F., 2005. Imaging the Indian subcontinent beneath the Himalaya. Nature 435, 1222–1225. http://dx.doi.org/10.1038/nature03678.

Stein, R.S., 1999. The role of stress transfer in earthquake occurrence. Nature 402 (6762), 605–609.

Stevens, V.L., Avouac, J.P., 2015. Interseismic coupling on the main Himalayan thrust. Geophys. Res. Lett. 42, 5828–5837. http://dx.doi.org/10.1002/2015GL064845.

Vannucchi, P., Sage, F., Phipps Morgan, J., Remitti, F., Collot, J.-Y., 2012. Toward a dynamic concept of the subduction channel at erosive convergent margins with implications for interplate material transfer. Geochem. Geophys. Geosyst. 13, Q02003. http://dx.doi.org/10.1029/2011GC003846.

von Huene, R., Scholl, D.W., 1991. Observations at convergent margins concerning sediment subduction, subduction erosion, and the growth of continental crust. Rev. Geophys. 29 (3), 279–316. http://dx.doi.org/10.1029/91RG00969.

Wakabayashi, J., Rowe, C.D., 2015. Whither the megathrust? Localization of large-scale subduction slip along the contact of a mélange. Int. Geol. Rev. 57 (5–8), 854–870. http://dx.doi.org/10.1080/00206814.2015.1020453.

Waldhauser, F., Ellsworth, W.L., 2000. A double-difference earthquake location algorithm: method and application to the northern Hayward Fault, CA. Bull. Seismol. Soc. Am. 90, 1353–1368.

Wang, K., Fialko, Y., 2015. Slip model of the 2015 Mw7.8 Gorkha (Nepal) earthquake from inversions of ALOS-2 and GPS data. Geophys. Res. Lett. 42 (18), 7452–7458. http://dx.doi.org/10.1002/2015GL065201.

Zhang, G., Hetland, E., Xinjian, S., 2015. Slip in the 2015 Mw7.9 Gorkha and Mw 7.3 Kodari, Nepal, earthquakes revealed by seismic and geodetic data: delayed slip in the Gorkha and slip deficit between the two earthquakes. Seismol. Res. Lett. 86 (6), 1578–1586. http://dx.doi.org/10.1785/0220150139.